

Heat-transfer fingerprint of Josephson breathers

Duilio De Santis ^{1,*} Bernardo Spagnolo ^{1,2,†} Angelo Carollo ^{1,‡} Davide Valenti ^{1,§} and Claudio Guarcello ^{3,4,¶}

¹*Dipartimento di Fisica e Chimica “E. Segrè”, Group of Interdisciplinary Theoretical Physics, Università degli Studi di Palermo, I-90128 Palermo, Italy*

²*Radiophysics Department, Lobachevsky State University, 603950 Nizhniy Novgorod, Russia*

³*Dipartimento di Fisica “E. R. Caianiello”, Università degli Studi di Salerno, I-84084 Fisciano, Salerno, Italy*

⁴*INFN, Sezione di Napoli, Gruppo Collegato di Salerno - Complesso Universitario di Monte S. Angelo, I-80126 Napoli, Italy*

(Dated: June 2, 2023)

A sine-Gordon breather enhances the heat transfer in a thermally biased long Josephson junction. This solitonic channel allows for the tailoring of the local temperature throughout the system. Furthermore, the phenomenon implies a clear thermal fingerprint for the breather, and thus a ‘non-destructive’ breather detection strategy is proposed here. Distinct breathing frequencies result in morphologically different local temperature peaks, which can be identified in an experiment.

I. INTRODUCTION

The soaring development of quantum technologies continuously propels the field of thermodynamics towards new fundamental and applied challenges, such as the accurate heat management at the nanoscale [1, 2]. This is the goal of *caloritronics* [3–5], whose interest has been revived after the recent experimental demonstration of the phase-coherent control of the thermal transport in Josephson devices [6, 7]. Superconducting phase coherence offers a unique knob for mastering heat flows. This feature has led researchers to conceive and implement nonlinear caloritronic devices for different applications, such as thermometry [8–10] and refrigeration [11–13], memories [14, 15] and engines [16, 17], routers [18–20] and switches [21], diffractors [22] and radiation detectors [23, 24]. The strength of *phase-coherent caloritronics* lies in the feasibility of adjusting the temperature by controlling the Josephson phase, e.g., via externally applied magnetic fields.

Extended Josephson systems, such as long Josephson junctions (LJJs) [25], constitute an established research topic in applied superconductivity, thanks to their richness in terms of both physical phenomena and cutting-edge applications [26–30]. From the viewpoint of thermal transport, the behavior of these devices is, however, largely unknown [31–33]. It is then important to ask: can heat flows represent a new paradigm in such a context? Can this provide unprecedented means to experimentally investigate complex scenarios which have remained beyond reach for many years?

In this work, a fresh perspective is brought to the study of Josephson breathers, i.e., kink-antikink (or fluxon-antifluxon) oscillating bound states [34, 35]. These excitations, which are notoriously hard to trace via standard

techniques in the field of LJJs [36–41], are shown to alter the heat transport in thermally biased junctions. The mastering of the local temperature within the system can thus be achieved via breathers, an intriguing fact which enhances their physical relevance. In addition, this unveiled property naturally sets the stage for a long sought non-destructive breather detection scheme, i.e., a protocol not involving the mode’s breakup. Morphologically different local thermal profiles are found at distinct oscillation frequencies. The latter fact is useful in view of experiments and is a consequence of the analytical sine-Gordon (SG) breather waveform. By exploiting noise and ac driving for the excitation and the stabilization of the nonlinear breathing states [41], the robustness of the thermal fingerprint is demonstrated as well.

II. THE MODEL

The dynamics of the LJJ is described via the perturbed SG equation for the Josephson phase $\varphi(\mathcal{X}, \mathcal{T})$ [25]

$$\frac{\partial^2 \varphi}{\partial \mathcal{X}^2} - \frac{\partial^2 \varphi}{\partial \mathcal{T}^2} - \alpha \frac{\partial \varphi}{\partial \mathcal{T}} = \sin \varphi - \eta \sin[\omega(\mathcal{T} - \mathcal{T}_0)] - \gamma_n(\mathcal{X}, \mathcal{T}), \quad (1)$$

which is written in terms of dimensionless space and time variables, i.e., $\mathcal{X} = x/\lambda_J$ and $\mathcal{T} = t\omega_p$. Here, the characteristic scales are given by the Josephson penetration depth $\lambda_J = \sqrt{\Phi_0/(2\pi\mu_0 t_d J_c)}$ and the Josephson plasma frequency $\omega_p = \sqrt{2\pi J_c/(\Phi_0 C)}$ [25], where t_d is the effective magnetic thickness, $J_c = I_c/A$ the Josephson critical current per unit area [with $A = L \times W$ being the junction’s area, and L (W) its length (width)], and C the junction’s specific capacitance (Φ_0 and μ_0 are the magnetic flux quantum and the vacuum permeability, respectively). Furthermore, in Eq. (1), $\alpha = 1/(\omega_p R_a C)$ is the damping coefficient (where R_a indicates the normal resistance per area), ω (η) is the frequency (amplitude) of the external ac driving in units of ω_p (I_c), \mathcal{T}_0 is a normalized time displacement, and $\gamma_n(\mathcal{X}, \mathcal{T})$ is a dimensionless noise current with zero average and autocorrelation func-

* duilio.desantis@unipa.it

† bernardo.spagnolo@unipa.it

‡ angelo.carollo@unipa.it

§ davide.valenti@unipa.it

¶ cguarcello@unisa.it

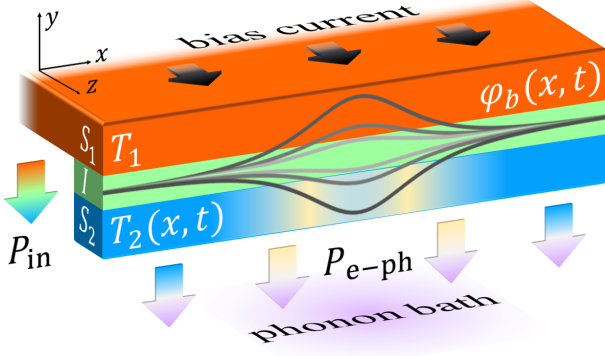


FIG. 1. Pictorial view of an overlap-geometry, current-driven LJJ, in the presence of a thermal bias. The temperature T_1 of the first electrode (S_1) is fixed, whereas S_2 has a floating temperature $T_2(x, t)$. The latter electrode is also in thermal contact with a phonon bath at temperature T_b . For $T_1 > T_2(x, t) \geq T_b$, the thermal power $\mathcal{P}_{\text{in}}(T_1, T_2, \varphi, V)$ coming into S_2 is depicted, along with the outgoing term $\mathcal{P}_{\text{e-ph}}(T_2, T_b)$, which is due to S_2 's quasiparticles coupling with the lattice phonons at T_b . Lastly, the drawing illustrates the double-peaked local heating in S_2 caused by the breather oscillations, quantitatively discussed below.

tion given by

$$\langle \gamma_n(\mathcal{X}_1, \mathcal{T}_1) \gamma_n(\mathcal{X}_2, \mathcal{T}_2) \rangle = 2\alpha\Gamma\delta(\mathcal{X}_1 - \mathcal{X}_2)\delta(\mathcal{T}_1 - \mathcal{T}_2). \quad (2)$$

The noise strength $\Gamma = 2\pi\mathcal{L}k_B T / (\Phi_0 I_c)$ is proportional to the normalized junction length $\mathcal{L} = L/\lambda_J$ and the absolute temperature T (k_B is the Boltzmann constant). For an overlap-geometry LJJ, see Fig. 1, and null external magnetic fields, the imposed boundary conditions are $(\partial\varphi/\partial\mathcal{X})|_{\mathcal{X}=0,\mathcal{L}} = 0$.

Figure 1 presents a sketch of the temperature-biased setup examined here, as well as the double-peaked local heating due to the breather oscillations. Specifically, the temperature T_1 of the first electrode (S_1) is fixed, while S_2 has a floating temperature $T_2(x, t)$ [42]. The latter electrode is also in thermal contact with a phonon bath at known temperature T_b , and the relation $T_1 > T_2(x, t) \geq T_b$ holds. The spatio-temporal behavior of the floating temperature is modeled by the diffusion equation [31]

$$\frac{\partial}{\partial x} \left[\kappa(T_2) \frac{\partial T_2}{\partial x} \right] + \mathcal{P}_{\text{tot}}(T_1, T_2, T_b, \varphi, V) = c_v(T_2) \frac{\partial T_2}{\partial t}, \quad (3)$$

where $\kappa(T_2)$ is the electronic heat conductivity [43], $\mathcal{P}_{\text{tot}}(T_1, T_2, T_b, \varphi, V) = \mathcal{P}_{\text{in}}(T_1, T_2, \varphi, V) - \mathcal{P}_{\text{e-ph}}(T_2, T_b)$, with $\mathcal{P}_{\text{in}}(T_1, T_2, \varphi, V)$ and $\mathcal{P}_{\text{e-ph}}(T_2, T_b)$ being, respectively, the ingoing and outgoing thermal power densities in S_2 [$V \equiv V(x, t)$ is the voltage drop] [44], see Fig. 1, and $c_v(T_2)$ is the volume-specific heat capacity. Note that the LHS of Eq. (3) describes the heat's spatial diffusion, while its RHS represents the variation of S_2 's internal energy.

The phase-dependent 'in' thermal power density is

structured as follows [33]

$$\mathcal{P}_{\text{in}}(T_1, T_2, \varphi, V) = \mathcal{P}_{\text{qp}}(T_1, T_2, V) - \cos\varphi \mathcal{P}_{\text{cos}}(T_1, T_2, V). \quad (4)$$

Here, the 'qp' term is a quasiparticle contribution, i.e., it amounts to an S_1 (hot) $\rightarrow S_2$ (cold) incoherent energy flow, whereas the 'cos' term stems from the energy-carrying tunneling events involving the destruction and recombination of Cooper pairs in both S_1 and S_2 [45, 46].

The initial condition for Eq. (3) is $T_2|_{t=0} = T_b$, and the edges of the device are assumed to be thermally isolated, implying $(\partial T_2/\partial x)|_{x=0,L} = 0$.

Detailed information regarding all the above expressions, including their physical significance and the numerical means to handle them, is given in Apps. A and B. In what follows, an LJJ composed by Nb/ AlO_x /Nb is considered, with $L = 300 \mu\text{m}$, $W = 0.5 \mu\text{m}$, $d_2 = 0.1 \mu\text{m}$ (thickness of S_2), $d = 1 \text{ nm}$ (thickness of the insulating layer), $R_a = 50 \Omega \mu\text{m}^2$, and $C = 100 \text{ fF } \mu\text{m}^{-2}$. Such a device is thermally biased by setting $T_1 = 7 \text{ K}$ and $T_b = 4.2 \text{ K}$ [31]. As shown in App. C, by accounting for the temperature dependence in both $t_d(T_1, T_2)$ and $I_c(T_1, T_2)$, one can estimate the values [47] $\lambda_J \approx 8 \mu\text{m}$ (thus $\mathcal{L} = L/\lambda_J \approx 37$), $\omega_p \approx 0.95 \text{ THz}$, $\alpha \approx 0.2$, and $\Gamma \approx 0.0026$ [48]. Before proceeding, it should be also stressed that the overall features found below apply to a wide range of parameter values. The currently chosen set is just meant to provide a realistic example.

III. BREATHER-ENHANCED THERMAL TRANSPORT

The effects of breathers on the evolution of the temperature $T_2(\mathcal{X}, \mathcal{T})$ are studied in the following way. First, the electrode S_2 is allowed to fully thermalize in the absence of excitations, e.g., by taking $\varphi(\mathcal{X}, \mathcal{T} < \mathcal{T}_0)$ in an unperturbed scenario. Equation (1) is then solved for $\mathcal{T}_0 \leq \mathcal{T} \leq \mathcal{T}_f$, and the generation of a stabilized breather centered at $\mathcal{X} = \mathcal{X}_0$ is mimicked by imposing $\varphi|_{\mathcal{T}=\mathcal{T}_0} = \varphi^0|_{\mathcal{T}=\mathcal{T}_0}$ and $(\partial\varphi/\partial\mathcal{T})|_{\mathcal{T}=\mathcal{T}_0} = (\partial\varphi^0/\partial\mathcal{T})|_{\mathcal{T}=\mathcal{T}_0}$, with $\varphi^0(\mathcal{X}, \mathcal{T}) = \varphi_b(\mathcal{X}, \mathcal{T}) + \varphi_v(\mathcal{T})$ being the 'breather plus vacuum' state [49]

$$\varphi^0(\mathcal{X}, \mathcal{T}) = 4 \operatorname{atan} \left\{ \frac{\sqrt{1-\omega^2} \cos[\omega(\mathcal{T} - \mathcal{T}_0) + \pi - 2\theta]}{\omega \cosh[\sqrt{1-\omega^2}(\mathcal{X} - \mathcal{X}_0)]} \right\} + \frac{\eta \sin[\omega(\mathcal{T} - \mathcal{T}_0) - \theta]}{\sqrt{(1-\omega^2)^2 + \alpha^2\omega^2}}, \quad \tan\theta = \frac{\alpha\omega}{1-\omega^2}, \quad (5)$$

which is known to lock to an ac force of suitable amplitude, i.e., for $\eta \approx \eta_{\text{th}}(\omega) = \frac{2\alpha(1-\omega^2) \operatorname{asin}\sqrt{1-\omega^2}}{K(1-\omega^2) - E(1-\omega^2)}$ (K and E are, respectively, complete elliptic integrals of the first and the second kind) [49]. The choices $x_0 = \mathcal{X}_0\lambda_J = 150 \mu\text{m}$, $t_0 = \mathcal{T}_0/\omega_p = 2 \text{ ns}$, and $t_f = \mathcal{T}_f/\omega_p = 10 \text{ ns}$ are made. It is worth adding that

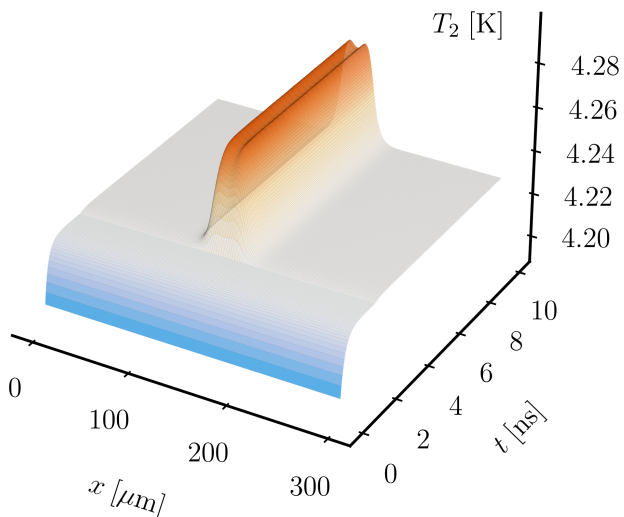


FIG. 2. Spatio-temporal view of the temperature T_2 . The generation of a stabilized breather centered at $x_0 = 150 \mu\text{m}$ is mimicked at $t_0 = 2 \text{ ns}$, that is, after S_2 has thermalized at the steady value of $\sim 4.23 \text{ K}$. The plot displays the double-peaked local heating, with $\max\{T_2\} \gtrsim 4.27 \text{ K}$, caused by the breather. Parameter values: $\omega = 0.5$, $\eta = 0.33$, and $\Gamma = 0$.

the below long-time temperature behaviors do not depend on the value of the excitation-free thermalization time t_0 .

Setting $\Gamma = 0$, a typical simulation outcome for $T_2(x, t)$ is shown in Fig. 2 for $\omega = 0.5$ and $\eta = 0.33 \approx \eta_{\text{th}}(\omega = 0.5)$. One can first appreciate the temperature's relaxation towards the (excitation-free) steady value of $\sim 4.23 \text{ K}$ within $t = t_0$. Strikingly, for $t > t_0$, a local exponential growth of the temperature is observed in correspondence to the breather, leading to a persisting double-peaked local heating, with $\max\{T_2\} \gtrsim 4.27 \text{ K}$. Such a profile is a natural consequence of the breather being a two-soliton bound state. A clear thermal fingerprint for the breather is thus brought to light. The latter mode is indeed notoriously hard to track via mean voltage measurements due to its fast (zero-averaging) oscillations, and the few proposals currently available in the literature resort to the breather's destruction for probing purposes [36, 38, 41]. By virtue of the characteristic ' $\cos \varphi$ ' dependence in Eq. (4), the breather's influence within the thermal realm is nonvanishing, and the detection does not require its breakup—a fact which makes this framework particularly appealing.

It follows from the analytical SG breather solution, see Eq. (5), that the mode's morphology, e.g., its oscillation amplitude and width, encodes information on the breathing frequency [34, 35]. It is hence reasonable to expect differently shaped thermal profiles for distinct frequencies, with lower ω values yielding more pronounced double-peaked patterns (since the corresponding breathers are closer to unbound kink-antikink

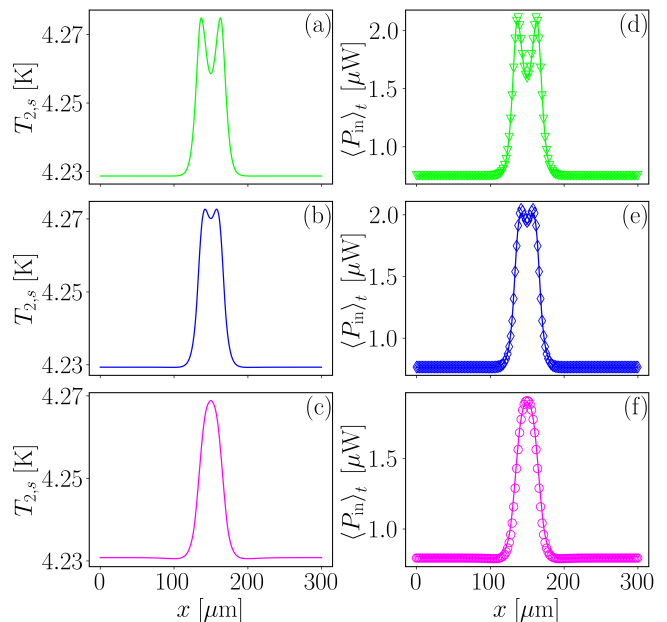


FIG. 3. Panels (a)-(c): Stationary temperature curves ($T_{2,s}$) at different breather frequencies. Panels (d)-(f): Time-averaged thermal powers $\langle P_{\text{in}} \rangle_t$ corresponding to the simulations from panels (a)-(c) (lines) and their analytical counterparts, i.e., $\langle P_{\text{in}}(T_1, T_b, \varphi^0, V^0) \rangle_t$ (triangles, diamonds, and circles). In the panels, $\Gamma = 0$ is set, and the green, blue, and purple colors stand for the combinations $\omega = 0.3$ and $\eta = 0.3$, $\omega = 0.5$ and $\eta = 0.33$, and $\omega = 0.7$ and $\eta = 0.31$, respectively.

pairs). This is confirmed in Fig. 3(a)-(c), which displays three stationary temperature curves ($T_{2,s}$) at different breather frequencies. Here, the green, blue, and purple lines are obtained, respectively, for $\omega = \{0.3, 0.5, 0.7\}$ and $\eta = \{0.3, 0.33, 0.31\}$, where $\eta \approx \eta_{\text{th}}(\omega)$. Note that in the low-frequency representative case a markedly double-peaked waveform emerges, with $\max\{T_{2,s}\} \gtrsim 4.27 \text{ K}$, while in the high-frequency one the resulting curve is essentially bell-shaped, with $\max\{T_{2,s}\} \lesssim 4.27 \text{ K}$. The result at $\omega = 0.5$ is somewhat in between the previous two, as one may guess. Far from electrode's center, $T_{2,s} \sim 4.23 \text{ K}$ is obtained in all scenarios.

As hinted above, the temperature's envelope reflects the behavior of the thermal power P_{in} . This structural analogy is clearly demonstrated through Fig. 3(d)-(f), where the lines indicate the time-averaged thermal powers $\langle P_{\text{in}} \rangle_t$ [50] relative to the simulations of Eq. (1) and Eq. (3) discussed in panels (a)-(c). In particular, the local enhancement of the average thermal power is higher for the prominent double-peaked (green) profile, for which $\max\{\langle P_{\text{in}} \rangle_t\} \gtrsim 2 \mu\text{W}$, whereas the bell-shaped (purple) one is characterized by $\max\{\langle P_{\text{in}} \rangle_t\} \lesssim 2 \mu\text{W}$. The $\omega = 0.5$ (blue) outcome falls once again in between the prior two. In all cases, $\langle P_{\text{in}} \rangle_t \lesssim 1 \mu\text{W}$ is observed away from the breather.

Figure 3(d)-(f) features also a comparison between the above mentioned $\langle P_{\text{in}} \rangle_t$ curves and their analyti-

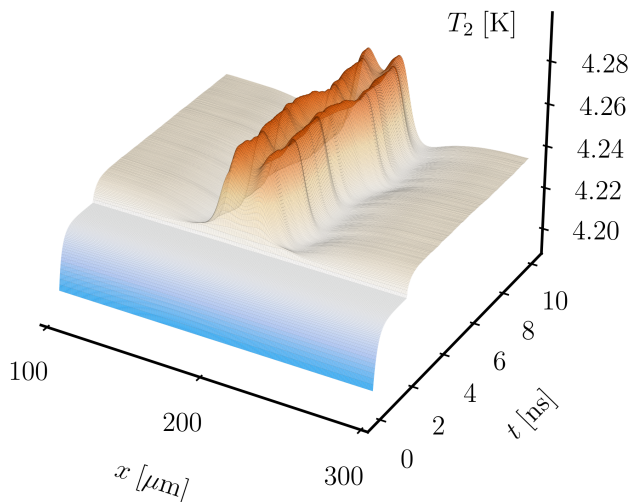


FIG. 4. Spatio-temporal view of the temperature T_2 . A noise-induced and ac-locked breather, centered roughly at $200 \mu\text{m}$, is observed for $t \gtrsim t_0 = 2 \text{ ns}$, i.e., after S_2 's thermalization at the steady value of $\sim 4.23 \text{ K}$ has occurred. Focusing on the region $[100, 300] \mu\text{m}$, the breather is shown to induce a double-peaked local heating, with $\max\{T_2\} \gtrsim 4.27 \text{ K}$. Parameter values: $\omega = 0.6$, $\eta = 0.59$, and $\Gamma = 0.0026$.

cal counterparts. More specifically, the green triangles ($\omega = 0.3$), the blue diamonds ($\omega = 0.5$), and the purple circles ($\omega = 0.7$) are calculated directly from Eq. (5) as $\langle P_{\text{in}}(T_1, T_b, \varphi^0, V^0) \rangle_t$, with $V^0 = [\Phi_0/(2\pi)] (\partial\varphi^0/\partial t)$ being the voltage profile associated to φ^0 , without using Eqs. (1) and (3). The great accord displayed is yet another indication that the unveiled phenomenology can be rigorously ascribed to the breather waveform.

IV. NOISE-INDUCED BREATHERS

Pairing the revealed thermal fingerprint with a reliable breather excitation and stabilization technique is an important task in view of an experimental detection. To this end, it has been recently established that the combination of noise and ac forcing can lead to the emergence of long-time stable breather modes in random locations [41].

In the simulation shown in Fig. 4, the noisy junction ($\Gamma = 0.0026$, see Sec. II) is driven with the frequency/amplitude combination $\omega = 0.6$ and $\eta = 0.59$ [41]. After the excitation-free thermalization of the electrode S_2 for $t < t_0$, a noise-induced and ac-locked breather arises close to $200 \mu\text{m}$, which motivates the plot's focus on the region $[100, 300] \mu\text{m}$. Interestingly, the distinctive traits of the breather's influence on the temperature T_2 are preserved even in the stochastic scenario. As one expects, now the position of the solitonic state's center slightly fluctuates in time, along with its amplitude, but the overall behavior is analogous to that presented in Fig. 2. A double-peaked local heating,

with $\max\{T_2\} \gtrsim 4.27 \text{ K}$, is indeed clearly seen. In short, noisy and ac-driven LJJ's represent natural candidates for unveiling the breather's thermal fingerprint, which is non-destructive.

V. CONCLUSIONS

It is demonstrated that SG breathers enhance the heat transfer in thermally biased, overlap-geometry LJJ's. This brings to light a soliton-based mechanism for mastering the local temperature within the system. Another important point is that this effect allows for the design of a non-destructive breather detection strategy. Notably, distinct breathing frequencies yield morphologically different local temperature peaks, which are well understood in terms of the analytical SG breather profile and can be experimentally identified. To illustrate the robustness of the results, this work pairs the above thermal fingerprint with a reliable breather and stabilization technique, via the combined action of noise and ac driving [41].

The developed ideas are expected to find application even beyond the LJJ device. In particular, it seems reasonable to look at discrete systems, and exploit a similar approach to study and probe, for example, the elusive oscillobreather states in parallel arrays of thermally biased superconducting junctions [51]. Furthermore, a connection between the present scenario and the more general context of soliton-sustained heat propagation in various devices, such as wires and nanotubes [52, 53], naturally comes to mind.

Appendix A: Modelling of the thermally biased long Josephson junction

To model the evolution of the floating temperature, one should discuss the typical length scale for thermalization within the electrode. In the diffusive regime, the inelastic scattering length can be considered $l_{\text{in}} = \sqrt{\tau_s \mathcal{D}} \approx 0.3 \mu\text{m}$ for Nb at 4.2 K, where τ_s is the quasiparticle scattering lifetime and $\mathcal{D} = \sigma_N / (e^2 N_F)$ is the diffusion constant, with σ_N and N_F being, respectively, the electrical conductivity in the normal state and the density of states at the Fermi energy (e is the electron charge). Since exclusively the junction length L is much larger than l_{in} , S_2 essentially behaves as a 1-d diffusive superconductor, and Eq. (3) holds [31]. Furthermore, in Eq. (3), the electronic heat conductivity $\kappa(T_2)$ reads [43]

$$\kappa(T_2) = \frac{\sigma_N}{2e^2 k_B T_2^2} \int_{-\infty}^{+\infty} \varepsilon^2 \cos^2 \left\{ \text{Im} \left[\text{arctanh} \left(\frac{\Delta(T_2)}{\varepsilon + i\gamma} \right) \right] \right\} \times \frac{d\varepsilon}{\cosh^2 \left(\frac{\varepsilon}{2k_B T_2} \right)} \quad (\text{A1})$$

Here, the BCS-like superconducting gap $\Delta(T) = \Delta \tanh\left(1.74\sqrt{T_c/T - 1}\right)$ is employed [54], with $\Delta = 1.764k_B T_c$, $T_c = 9.2$ K being the critical temperature for Nb, and $\gamma = 10^{-4}\Delta$ the Dynes broadening parameter [55].

In the adiabatic limit, i.e., when $eV \ll \min\{k_B T_1, k_B T_2, \Delta(T_1), \Delta(T_2)\}$, one can write [46]

$$\begin{aligned} \mathcal{P}_{\text{qp}}(T_1, T_2, V) &= \frac{1}{e^2 R_a d_2} \int_{-\infty}^{+\infty} \mathcal{N}(\varepsilon - eV, T_1) \\ &\times \mathcal{N}(\varepsilon, T_2) (\varepsilon - eV) \\ &\times [f(\varepsilon - eV, T_1) - f(\varepsilon, T_2)] d\varepsilon \end{aligned} \quad (\text{A2})$$

and

$$\begin{aligned} \mathcal{P}_{\text{cos}}(T_1, T_2, V) &= \frac{1}{e^2 R_a d_2} \int_{-\infty}^{+\infty} \mathcal{N}(\varepsilon - eV, T_1) \\ &\times \mathcal{N}(\varepsilon, T_2) \frac{\Delta(T_1)\Delta(T_2)}{\varepsilon} \\ &\times [f(\varepsilon - eV, T_1) - f(\varepsilon, T_2)] d\varepsilon, \end{aligned} \quad (\text{A3})$$

in which $\mathcal{N}(\varepsilon, T) = \left| \text{Re} \left[\frac{\varepsilon + i\gamma}{\sqrt{(\varepsilon + i\gamma)^2 - \Delta(T)^2}} \right] \right|$ is the reduced superconducting density of state, and $f(\varepsilon, T) = [1 + e^{\varepsilon/(k_B T)}]^{-1}$ is the Fermi distribution function. The breather oscillations quickly average to zero voltage, i.e., $\langle V_b \rangle_t \approx 0$ is observed over times much smaller than the characteristic time of Eq. (3), thus satisfying the above adiabatic condition. Furthermore, it should be emphasized that the essence of the phenomenology, that is, the thermal profiles discussed in the main text (Figs. 2-4), lies in the cosine φ -dependence alone.

The ‘e-ph’ thermal power density accounts for the energy exchange between electrons and phonons in the superconductor, and it is given by [44]

$$\begin{aligned} \mathcal{P}_{\text{e-ph}} &= \frac{-\Sigma}{96\zeta(5)k_B^5} \int_{-\infty}^{+\infty} E dE \int_{-\infty}^{+\infty} \varepsilon^2 \text{sign}(\varepsilon) M_{E, E+\varepsilon} \\ &\times \left\{ \coth\left(\frac{\varepsilon}{2k_B T_b}\right) [\mathcal{F}(E, T_2) - \mathcal{F}(E + \varepsilon, T_2)] \right. \\ &\left. - \mathcal{F}(E, T_2)\mathcal{F}(E + \varepsilon, T_2) + 1 \right\} d\varepsilon, \end{aligned} \quad (\text{A4})$$

where Σ is the electron-phonon coupling constant, ζ is the Riemann zeta function, $M_{E, E'} = \mathcal{N}(E, T_2)\mathcal{N}(E', T_2) [1 - \Delta(T_2)^2/(EE')]$, and $\mathcal{F}(\varepsilon, T_2) = \tanh[\varepsilon/(2k_B T_2)]$. Here, the lattice phonons of the superconductor are assumed to be thermalized with the substrate residing at T_b by virtue of the vanishing Kapitza resistance between the thin metallic films and the substrate at low temperatures [1].

The RHS of Eq. (3) involves $c_v(T_2) = T_2 (d\mathcal{S}/dT_2)$, which is defined in terms of the electronic entropy density

of S_2 [12]

$$\begin{aligned} \mathcal{S}(T_2) &= -4k_B N_F \int_0^{+\infty} \mathcal{N}(\varepsilon, T_2) \{ [1 - f(\varepsilon, T_2)] \\ &\times \ln [1 - f(\varepsilon, T_2)] + f(\varepsilon, T_2) \ln f(\varepsilon, T_2) \} d\varepsilon. \end{aligned} \quad (\text{A5})$$

The following parameter values are considered: $\sigma_N = 6.7 \times 10^6 \Omega^{-1} \text{m}^{-1}$, $N_F = 10^{47} \text{J}^{-1} \text{m}^{-3}$, and $\Sigma = 3 \times 10^9 \text{W m}^{-3} \text{K}^{-5}$.

To conclude, it is perhaps worth mentioning that the present framework can be rephrased to apply for junctions involving non-identical electrodes as well.

Appendix B: Numerical details

Implicit finite-difference schemes are used to solve both the perturbed SG equation and the diffusion equation, keeping the same spatio-temporal grid in the two cases. In particular, the spatial domain is divided into \mathcal{N} cells of length Δx and the temporal domain into \mathcal{M} intervals of duration Δt . The perturbed SG equation is handled in the same way as in Ref. [41], see its Supplemental Material for a complete account of this matter. In Eq. (3), indicating the space-time restriction of $T_2(x, t)$ as $(T_2)_n^m = T_2(n \Delta x, m \Delta t)$, for $n = 1, \dots, \mathcal{N}$ and $m = 1, \dots, \mathcal{M}$, the derivatives are [56]

$$\begin{aligned} \frac{\partial T_2}{\partial x} &\approx \frac{1}{2\Delta x} [(T_2)_{n+1}^m - (T_2)_{n-1}^m], \\ \frac{\partial T_2}{\partial t} &\approx \frac{1}{\Delta t} [(T_2)_n^{m+1} - (T_2)_n^m], \\ \frac{\partial^2 T_2}{\partial x^2} &\approx \frac{1}{2\Delta x^2} [(T_2)_{n+1}^{m+1} - 2(T_2)_n^{m+1} + (T_2)_{n-1}^{m+1} \\ &\quad + (T_2)_{n+1}^m - 2(T_2)_n^m + (T_2)_{n-1}^m]. \end{aligned} \quad (\text{B1})$$

By also applying both the initial and the boundary conditions, a tridiagonal system of equations is obtained. The latter’s resolution, achievable through, e.g., the Thomas’ algorithm [57], determines the unknown values $(T_2)_n^{m+1}$, given the previous ones $(T_2)_n^m$, with $n = 1, \dots, \mathcal{N}$. Throughout the work, the values of the discretization steps are $\Delta x = 0.4 \mu\text{m}$ and $\Delta t = 0.01$ ps (i.e., $\Delta\mathcal{X} = \Delta x/\lambda_J = 0.05$ and $\Delta\mathcal{T} = \Delta t \omega_p = 0.01$).

There is one more technical aspect concerning the solution of Eq. (3), that is, the T_2 -dependent integrals in Eqs. (A1)-(A5). At each time step of the implicit scheme, in principle, one would need to numerically compute the latter objects by using the instantaneous T_2 temperature profile [note that Eqs. (A2)-(A3) also depend on the instantaneous voltage]. Given the time-consuming nature of this task, another approach is pursued here. Via preliminary testing, very refined grids covering the entire variation range of the required quantities, i.e., T_2 and V , are constructed to evaluate all the integrals beforehand. These results are stored, and subsequently (if needed) standard interpolation routines are called to fill the gaps. The use of `scipy’s integrate.quad` (which is

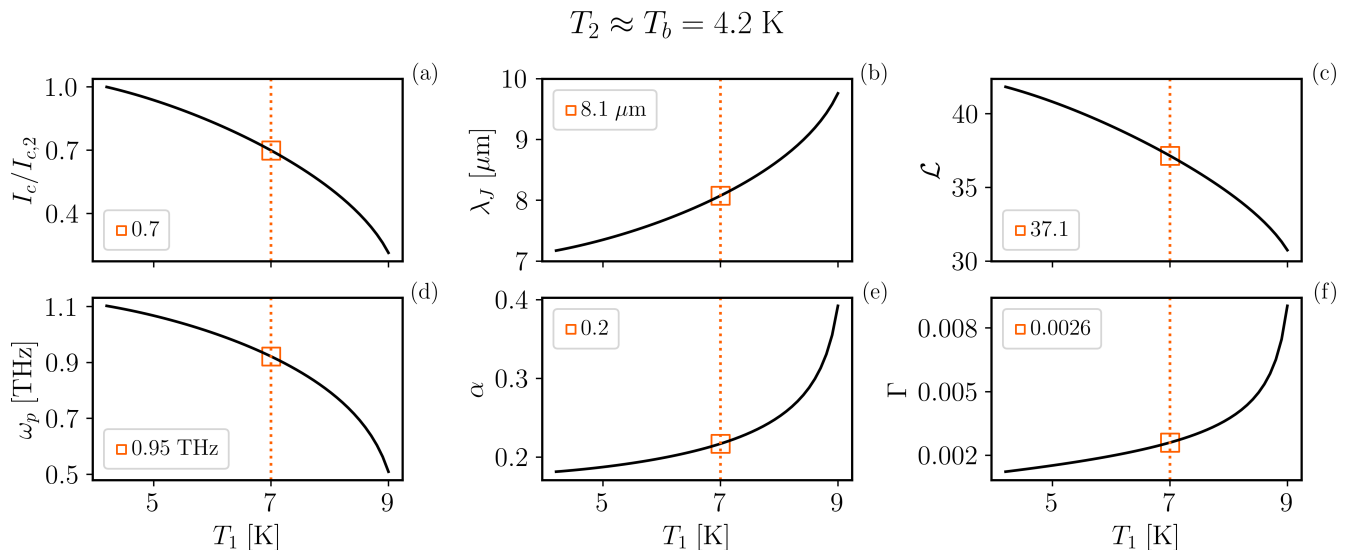


FIG. 5. Josephson critical current I_c in units of $I_{c,2} = I_c(T_2, T_2)$ [panel (a)], Josephson penetration depth λ_J [panel (b)], normalized junction length \mathcal{L} [panel (c)], Josephson plasma frequency ω_p [panel (d)], dissipation coefficient α [panel (e)], and noise strength Γ [panel (f)] as a function of the temperature T_1 . Here, the approximation $T_2 = T_b = 4.2 \text{ K}$ is used, and the orange squares denote the parameter values at $T_1 = 7 \text{ K}$, i.e., those employed throughout the work.

based on the Fortran library QUADPACK), as well as its interpolation schedules, is acknowledged.

Appendix C: Sine-Gordon model in the thermally biased scenario: parameter values

The parameters introduced within the SG framework are influenced by the temperatures T_1 and T_2 , and therefore they must be set properly. In particular, the effective magnetic thickness is given by [7]

$$t_d(T_1, T_2) = \lambda_L(T_1) \tanh \left[\frac{d_1}{2\lambda_L(T_1)} \right] + \lambda_L(T_2) \tanh \left[\frac{d_2}{2\lambda_L(T_2)} \right] + d, \quad (\text{C1})$$

where $\lambda_L(T) = \frac{\lambda_L^0}{\sqrt{1-(T/T_c)^4}}$ is the London penetration depth, and d_i is the thickness of the electrode S_i . The above assumption of a fixed temperature T_1 amounts to consider a very large S_1 volume, thus $d_1 \gg \lambda_L(T_1)$ is taken, which yields

$$t_d(T_1, T_2) \approx \lambda_L(T_1) + \lambda_L(T_2) \tanh \left[\frac{d_2}{2\lambda_L(T_2)} \right] + d. \quad (\text{C2})$$

Moreover, the Ambegaokar-Baratoff relation holds for

the Josephson critical current

$$I_c(T_1, T_2) = \frac{1}{2eR} \left| \int_{-\infty}^{\infty} \{ \mathcal{F}(\varepsilon, T_1) \text{Re} [\mathfrak{F}(\varepsilon, T_1)] \text{Im} [\mathfrak{F}(\varepsilon, T_2)] + \mathcal{F}(\varepsilon, T_2) \text{Re} [\mathfrak{F}(\varepsilon, T_2)] \text{Im} [\mathfrak{F}(\varepsilon, T_1)] \} d\varepsilon \right|, \quad (\text{C3})$$

in which $R = R_a/A$ is the normal resistance, and $\mathfrak{F}(\varepsilon, T) = \frac{\Delta(T)}{\sqrt{(\varepsilon+i\gamma)^2 - \Delta(T)^2}}$ is the anomalous Green's function [10]. As a result, one gets the Josephson penetration depth $\lambda_J(T_1, T_2) = \sqrt{\Phi_0 / [2\pi\mu_0 t_d(T_1, T_2) J_c(T_1, T_2)]}$, the normalized junction length $\mathcal{L}(T_1, T_2) = L/\lambda_J(T_1, T_2)$, the Josephson plasma frequency $\omega_p(T_1, T_2) = \sqrt{2\pi J_c(T_1, T_2) / (\Phi_0 C)}$, the dissipation coefficient $\alpha(T_1, T_2) = 1/[\omega_p(T_1, T_2) R_a C]$, and the noise strength $\Gamma(T_1, T_2) = 2\pi \mathcal{L}(T_1, T_2) k_B T_1 / [\Phi_0 I_c(T_1, T_2)]$. Regarding the latter quantity, the explicit T_1 in the numerator indicates that the ‘worst-case’ noise scenario is being accounted for.

Using the approximation $T_2 = T_b = 4.2 \text{ K}$ (since T_2 's variations discussed in the paper are negligible for the present purpose), Fig. 5 displays I_c in units of $I_{c,2} = I_c(T_2, T_2)$ [panel (a)], λ_J [panel (b)], \mathcal{L} [panel (c)], ω_p [panel (d)], α [panel (e)], and Γ [panel (f)] versus the temperature T_1 . The orange squares denote the parameter values at $T_1 = 7 \text{ K}$, i.e., those employed throughout the work. Note also that, in addition to those listed above, the value $\lambda_L^0 = 80 \text{ nm}$ is assumed here.

ACKNOWLEDGMENTS

The authors acknowledge the support of the Italian Ministry of University and Research (MUR).

-
- [1] F. Giazotto, T. T. Heikkilä, A. Luukanen, A. M. Savin, and J. P. Pekola, *Rev. Mod. Phys.* **78**, 217 (2006).
- [2] J. P. Pekola and B. Karimi, *Rev. Mod. Phys.* **93**, 041001 (2021).
- [3] M. J. Martínez-Pérez, P. Solinas, and F. Giazotto, *J. Low Temp. Phys.* **175**, 813 (2014).
- [4] A. Fornieri and F. Giazotto, *Nat. Nanotechnol.* **12**, 944 (2017).
- [5] S.-Y. Hwang and B. Sothmann, *Eur. Phys. J.: Spec. Top.* **229**, 683 (2020).
- [6] F. Giazotto and M. J. Martínez-Pérez, *Nature* **492**, 401 (2012).
- [7] M. José Martínez-Pérez and F. Giazotto, *Nat. Commun.* **5**, 3579 (2014).
- [8] F. Giazotto, P. Solinas, A. Braggio, and F. S. Bergeret, *Phys. Rev. Appl.* **4**, 044016 (2015).
- [9] M. Zgirski, M. Foltyn, A. Savin, K. Norowski, M. Meschke, and J. Pekola, *Phys. Rev. Appl.* **10**, 044068 (2018).
- [10] C. Guarcello, A. Braggio, P. Solinas, and F. Giazotto, *Phys. Rev. Appl.* **11**, 024002 (2019).
- [11] P. P. Hofer, M. Perarnau-Llobet, J. B. Brask, R. Silva, M. Huber, and N. Brunner, *Phys. Rev. B* **94**, 235420 (2016).
- [12] P. Solinas, R. Bosisio, and F. Giazotto, *Phys. Rev. B* **93**, 224521 (2016).
- [13] S.-Y. Hwang, B. Sothmann, and D. Sanchez, arXiv preprint arXiv:2301.10826 (2023).
- [14] C. Guarcello, P. Solinas, A. Braggio, M. Di Ventra, and F. Giazotto, *Phys. Rev. Appl.* **9**, 014021 (2018).
- [15] N. Ligato, F. Paolucci, E. Strambini, and F. Giazotto, *Nat. Phys.* **18**, 627 (2022).
- [16] B. Scharf, A. Braggio, E. Strambini, F. Giazotto, and E. M. Hankiewicz, *Commun. Phys.* **3**, 198 (2020).
- [17] F. Cavaliere, L. Razzoli, M. Carrega, G. Benenti, and M. Sassetti, *iScience* **26**, 10.1016/j.isci.2023.106235 (2023).
- [18] G. F. Timossi, A. Fornieri, F. Paolucci, C. Puglia, and F. Giazotto, *Nano Lett.* **18**, 1764 (2018).
- [19] S.-Y. Hwang, F. Giazotto, and B. Sothmann, *Phys. Rev. Appl.* **10**, 044062 (2018).
- [20] M. Acciai, F. Hajiloo, F. Hassler, and J. Splettstoesser, *Phys. Rev. B* **103**, 085409 (2021).
- [21] B. Sothmann, F. Giazotto, and E. M. Hankiewicz, *New J. Phys.* **19**, 023056 (2017).
- [22] C. Guarcello, F. Giazotto, and P. Solinas, *Phys. Rev. B* **94**, 054522 (2016).
- [23] C. Guarcello, A. Braggio, P. Solinas, G. P. Pepe, and F. Giazotto, *Phys. Rev. Appl.* **11**, 054074 (2019).
- [24] F. Paolucci, arXiv preprint arXiv:2303.13928 (2023).
- [25] A. Barone and G. Paternò, *Physics and Applications of the Josephson Effect* (Wiley, New York, 1982).
- [26] J. J. Mazo and A. V. Ustinov, in *The sine-Gordon Model and its Applications*, edited by J. Cuevas-Maraver, P. G. Kevrekidis, and F. Williams (Springer International Publishing, 2014) pp. 155–175.
- [27] A. I. Braginski, *J. Supercond. Nov. Magn.* **32**, 23 (2019).
- [28] W. Wustmann and K. D. Osborn, *Phys. Rev. B* **101**, 014516 (2020).
- [29] M. Wildermuth, L. Powalla, J. N. Voss, Y. Schön, A. Schneider, M. V. Fistul, H. Rotzinger, and A. V. Ustinov, *Appl. Phys. Lett.* **120**, 112601 (2022).
- [30] R. M. Lewis and M. P. Frank, *IEEE Trans. Appl. Supercond.* **33**, 1 (2023).
- [31] C. Guarcello, P. Solinas, A. Braggio, and F. Giazotto, *Phys. Rev. Appl.* **9**, 034014 (2018).
- [32] C. Guarcello, P. Solinas, A. Braggio, and F. Giazotto, *Sci. Rep.* **8**, 1 (2018).
- [33] C. Guarcello, P. Solinas, F. Giazotto, and A. Braggio, *J. Stat. Mech.-Theory E* **2019**, 084006 (2019).
- [34] A. C. Scott, *Nonlinear Science: Emergence and Dynamics of Coherent Structures* (Oxford, 2003).
- [35] T. Dauxois and M. Peyrard, *Physics of Solitons* (Cambridge University Press, 2006).
- [36] D. R. Gulevich, M. B. Gaifullin, and F. V. Kusmartsev, *Eur. Phys. J. B* **85**, 24 (2012).
- [37] R. Monaco, *Wave Motion* **88**, 214 (2019).
- [38] D. De Santis, C. Guarcello, B. Spagnolo, A. Carollo, and D. Valenti, *Chaos Solitons Fractals* **158**, 112039 (2022).
- [39] D. De Santis, C. Guarcello, B. Spagnolo, A. Carollo, and D. Valenti, *Commun. Nonlinear Sci. Numer. Simul.*, 106736 (2022).
- [40] D. De Santis, C. Guarcello, B. Spagnolo, A. Carollo, and D. Valenti, *Chaos Solitons Fractals* **168**, 113115 (2023).
- [41] D. De Santis, C. Guarcello, B. Spagnolo, A. Carollo, and D. Valenti, *Chaos Solitons Fractals* **170**, 113382 (2023).
- [42] This can be achieved via optimization of the electrodes' volumes [31, 33].
- [43] A. Fornieri, G. Timossi, P. Virtanen, P. Solinas, and F. Giazotto, *Nat. Nanotechnol.* **12**, 425 (2017).
- [44] A. V. Timofeev, C. P. García, N. B. Kopnin, A. M. Savin, M. Meschke, F. Giazotto, and J. P. Pekola, *Phys. Rev. Lett.* **102**, 017003 (2009).
- [45] K. Maki and A. Griffin, *Phys. Rev. Lett.* **15**, 921 (1965).
- [46] D. Golubev, T. Faivre, and J. P. Pekola, *Phys. Rev. B* **87**, 094522 (2013).
- [47] The approximation $T_2 = T_b$ is made here, since T_2 's variations (discussed later in the work) are negligible for the sake of these calculations.
- [48] The latter quantity explicitly depends on the temperature T , see Eq. (2). To display the results' robustness even in the 'worst-case' noise scenario, the highest temperature within the system, i.e., $T = T_1$, is taken.
- [49] P. S. Lomdahl and M. R. Samuelsen, *Phys. Rev. A* **34**, 664 (1986).
- [50] The time average is intended for $t \geq t_0$, with the simulations' being performed in analogous fashion to that presented in Fig. 2.
- [51] J. J. Mazo and T. P. Orlando, *Chaos* **13**, 733 (2003).
- [52] M. Sciacca, F. Alvarez, D. Jou, and J. Bafaluy, *Int J. Heat Mass Tran.* **155**, 119809 (2020).
- [53] M. Sciacca, I. Carlomagno, and A. Sellitto, *Wave Motion* **113**, 102967 (2022).
- [54] K. Senapati, M. G. Blamire, and Z. H. Barber, *Nat. Mater.* **10**, 849 (2011).
- [55] R. C. Dynes, V. Narayanamurti, and J. P. Garno, *Phys. Rev. Lett.* **41**, 1509 (1978).
- [56] W. F. Ames, *Numerical Methods for Partial Differential Equations* (Academic press, 1977).

- [57] W. H. Press, S. A. Teukolsky, W. T. Vetterling, and B. P. Flannery, *Numerical Recipes in Fortran 77: The Art of Scientific Computing* (Cambridge University Press, 1992).